Implementation of a new laser set-up for magnetometry using Cs vapour cell

July 26, 2026

Internship report
Alexandre Bellon*

Supervisor:
Dr Lucas Lavoine†

Key-words: *Quantum optic, quantum mechanics, magnetometry, non-linear magneto-optic rotation, Larmor precession, spin, Cesium, Laser ,*

Abstract

This internship aimed at building and characterising a first atomic magnetometer to be used in the experimental chamber of the Chromium experiment, LPL. Firstly, we characterised, repaired, and fine-tuned the LASER source. Then, the absorption spectrum of the different cells at our disposal have been established. The absorption spectroscopic set-up has been implemented. To-be-implemented-Cs cell have been tested. Finally, several magnetometry designs have been explored theoretically.

*alexandre.bellon@ens-lyon.fr, Département de physique de l'ENS de Lyon
†lucas.lavoine@univ-paris13.fr, Chromium group, GQM team, Laboratoire de Physique des Lasers

Contents

Acknowledgment

I would like to thanks deeply Dr Lucas Lavoine, my supervisor, for his invaluable help and guidance during my internship that allowed me to learn so much and go deeper in this subject than I expected. I thank very much Pr. Laurent Vernac for his inspiring view on physics and experimentation that moved my limits further than ever before. I am moreover especially grateful to Dr Benjamin Pasquiou, Dr Fatima Rahmouni for their help in both technical and conceptual aspects of my internship, always with patience and kindness. I would like to thanks Esther Fromm, M2 intern going for her thesis (good luck!) for the numerous discussion we had. Furthermore, I would like to thank all the members of the Chromium experimentation team for their kind welcome, especially Dr Bruno Laburthe-Tolra the LPL director and member of Chromium team and Dr Martin Rober-de-Saint-Vincent, GQM group leader. More generally, every member of the GQM team and the mechanical, electrical, and optical workshops have been of invaluable help. Finally, I wanted to thanks Alexis Faivre, Matthieu Chiron and Antonin Alboussiere--Revol, classmates and friends from the Ecole normale supérieure for their participation in proof reading this report.

1 Introduction

In 1914 Bose in [1] exposed his idea of a model for the gas of photons. Einstein extended that idea to integer-spin particles and created the Bose-Einstein statistic. In 1938, Fritz London proposed what became Bose-Einstein Condensate (BEC) as a mechanism that explained superconductivity and super-fluidity [2]. A BEC is a type of condensate in which the majority of particles are in their ground state. First condensation was obtain in 1995 by Anderson, Ensher, Matthews, Wieman, Cornell from a Rubidium gas cooled at 170 nK [3], and by Davis, Mewes, Andrews, van Druten, Durfee, Kurn, Ketterle from a Sodium gas [4].

In 2008, a team from the Laboratoire de Physique des Lasers (LPL) reported a successful production of Chromium (Cr) Bose-Einstein Condensate [5]. The Cr condensation has been achieved for the first time in 2005 by Tilman Pfau's group at Stuttgart [6]. While alkali atoms only lead to contact interaction, Chromium with 6 electrons in its valence shell has an atomic spin of $S = 3$ leading to the presence of dipolar interactions [6]. Chromium is much more suitable for such a study. Indeed knowing that dipolar interactions evolves as μ^2, with $\mu_{Cr} = 6\mu_B$, dipole-dipole interactions are 36 times stronger compared to alkali gas. Studying quantum thermalisation of isolated quantum system in presence of dipolar interactions is the goal of the LPL Chromium's experiment. After nearly 20 years of exploitation [7, 8, 9], the Chromium team decided to rebuild this experiment with better probe and in order to produce a 2D BEC.

During the experiment, Ramsey-like sequence will be used to probe the collective spin state of the system. Such a sequence is depicted in figure 1. This measure is very sensitive to the transverse magnetic field. Indeed the time of no-interaction τ is very much related to the magnetic field. To be able to probe the phase-shift caused by the dipole-dipole interaction, one needs to know exactly the behaviour of the magnetic field during this no-interaction time to compute its duration. More precisely, during a Ramsey sequence, the spin will precess at Larmor pulsation ω_L (fixed by the B_{ext} magnetic field), the micro-wave field being the reference. Any difference between ω_L and ω_{MW} will lead to a phase shift. This shift is particularly difficult to estimate during the spin dynamic. It will eventually prevent us from applying the right pulse sequence in order to measure the collective spin component (S_x, S_y, S_z). It is the context in which I started my internship. I had to explore the implementation of a magnetometer within the experiment chamber to achieve a better monitoring of the magnetic field that applies on the Cr BEC and thus enabling a reliable information on the magnetic field for the τ-calibration.

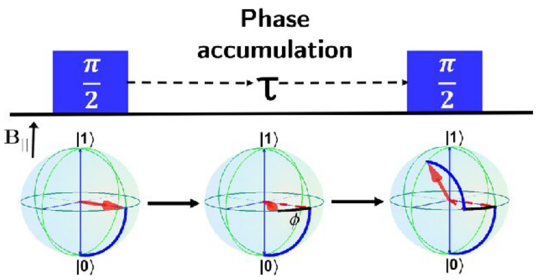

Figure 1: Ramsey sequence on the Bloch sphere. A first micro-wave (MW) $\pi/2$ pulse is applied to shift the atom that was in the ground state into an equatorial-superposition state. Then this states rotates during τ. After that time, another $\pi/2$ pulse is applied, the two-times rotated state then can be projected on the quantisation axis for read-out.

This report investigates the implementation of Optically-Pumped Magnetometer in a cost effective way aiming at integrating in the experiment chamber of the ultra-cold experimentation. First, we characterise, repair and fine-tune the 852nm LASER which was known to be lastly used in 2002. Following that, we establish the absorption spectrum of old and new Cesium cells and determine their pressure property. Then, we start to implement the atomic pumping and probing on a Cs vapour cell to accomplish magnetometry.

2 State of the art of magnetometry

Since the development of quantum mechanic, magnetometer field of application extended from industry [10, 11] to biomedical imaging and probing [12, 13, 14]. However, the main limitation to a wider use of such Optically Pumped Magnetometer (OPMs) is their low dynamic range making them very noise-sensitive. Recent breakthrough about that particular issue supported consequently this internship [15]. A quantity of methods have been developed adapting to a lot of constraints. Fabricant's article [16] is reporting a lot of those methods and is walking the interested reader through the step of the implementation of a magnetometer.

Three main method, described in [16] grabbed our attention. All of them use the atomic spin precession to probe the magnetic field. The first is the Free-Induction Decay, described by [17, 15]. The second is Bell-Bloom method, which foundational concept was given nearly 50 years ago in [18] and whose characterisation has been done around the year 2000 by [19]. More recently, the extension to an arbitrary direction of the magnetic field has been done in [20]. Finally, the Non-linear Magnetic Optical Rotation exploit the *Faraday Rotation* to probe the magnetic field [21, 22, 23].

However it is often that a highly shielded environment is used and little to no papers are interested in measuring near Gauss/ambient magnetic field. Although OPMs are recurrent in multiple field of physics, they have never been, to our knowledge, implemented or used in a ultra-cold experimentation nor under ultra-vacuum. Ultra-vacuum is typically needed for a BEC experimentation and is under 10^{-10}mbar. This experiment targets a 10^{-11}mbar vacuum.

3 Theoretical Aspects

3.1 LASER source

The Littman-Metclaf configuration (depicted in Fig.2) is a feed back configuration particularly adapted to the use of an external cavity diode LASER (ECDL). Two types of this configuration exists, we will focus on configuration of type I because it is the one that will be used in this study. A LASER diode is emitting towards a grating at grazing-incidence. The first order of diffraction is reflected by an adjustable mirror[1] that reflects the first order diffraction back on itself toward the grating. It is then diffracted once again, and the first order of that second diffraction provide optical feedback. The adjustable mirror thus close the LASER cavity.

[1] in general a retro-reflector or a similar optic system

The zero order diffraction is used as an output [24].

The grating being fixed, the tuning of the laser is done through the retro-reflector position. No movement of the output beam is hence observed. This configuration is providing less power than a Littrow configuration where the grating is movable and the output is the zero order of diffraction, making it slightly more powerful [25].

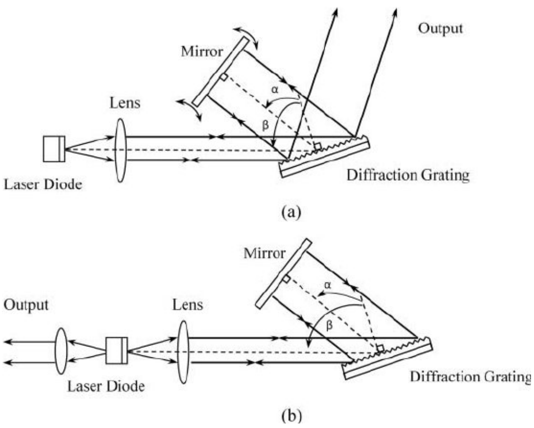

Figure 2: Littman-Metcalf configuration of type I (a) et II (b). Figure from [26].

3.2 Atomic magnetometry

Atomic magnetometry is achieved through two steps (generally), pumping and probing.

3.2.1 Atomic pumping

Atomic optical pumping corresponds to the general concept of using atomic transitions to prepare all the atoms in a specific state. We take [16] as the main source of information for this part alongside with the much more developed [27]. Now on, we will use the article from Daniel Steck as a reference for cesium atomic properties and numbers [28]. The atomic pumping transition we will be using is one between the triplet $F = 3 \rightarrow F' = 2, 3, 4$ and the triplets $F = 4 \rightarrow F' = 3, 4, 5$ [2].

Our goal in this study is to prepare the cesium atoms in a specific spin state. The absorption of a photon cannot address the electronic spin state of the atoms. Indeed, the quantum numbers of the atoms are affected following the selection rules [16]:

$$\Delta L = \pm 1, \tag{1}$$

$$\Delta S = 0, \tag{2}$$

$$\Delta J \in \{0, \pm 1\}, \tag{3}$$

$$\Delta F \in \{0, \pm 1\}, \tag{4}$$

and we see from equation 2 that the atomic spin cannot be changed by the absorption of a photon. In other words, the atomic spin is conserved in an atom-light interaction. However, the magnetic quantum number along a quantisation axis is changed by such an absorption. This depends on the light polarisation. This is stated by the following selection rule on the magnetic quantum number along the quantisation axis (which will be here the propagation axis) [16]:

$$\sigma_+ \rightarrow \Delta m_F = +1 \tag{5}$$

$$\sigma_- \rightarrow \Delta m_F = -1 \tag{6}$$

To prepare the atomic medium in spin coherent state, *e.g* to magnetise the cell, we have to polarise the LASER beam in σ_+ and to tune it on one of the absorption line. Both being of about the same optical depth, we can chose one or another. As suggested in [16, 27], such a process is counterbalanced by spontaneous decay of the atoms. The pumping rate is proportional to the beam's intensity [16]. The polarisation (or magnetisation) of the atomic medium is an equilibrium between the pumping rate Γ_p and the decay rate Γ_d. We should also take into account the maximum M_m magnetisation alongside z the quantification axis reachable in absence of relaxation. One can represent that process with the differential equation 7. Now on, M_x will represent the magnetisation along the x axis (resp. y, z).

[2] the transitions within the triplets being so close to each other (a few hundred of MHz) that we will address the two or three transitions of the same triplet at the same making them indistinguishable.

$$\frac{\mathrm{d}M_z}{\mathrm{d}t} = \Gamma_p(M_m - M_z) + \Gamma_d(-M_z) \quad (7)$$

On the two other axes, the pumping is lowering the global magnetisation along those axes to zero, spontaneous decay helping in that process:

$$\frac{\mathrm{d}M_{x,y}}{\mathrm{d}t} = \Gamma_p(-M_{x,y}) + \Gamma_d(-M_{x,y}) \quad (8)$$

To conclude, Fabricant in [16] is exhibiting an effective relaxation rate $\Gamma = \Gamma_p + \Gamma_d$ and a stady-state magnetisation $M_a = M_m \Gamma_p / \Gamma$ and compute:

$$\frac{\mathrm{d}}{\mathrm{d}t}\begin{pmatrix} M_x \\ M_y \\ M_z \end{pmatrix} = \Gamma \begin{pmatrix} -M_x \\ -M_y \\ M_a - M_z \end{pmatrix}. \quad (9)$$

Preparation of the atomic medium in a highly magnetised state is therefore possible and only parametrised by the beam's intensity if one use a $\sigma_\pm$ polarised beam at the transition frequency. It is important to note here that the transition lines are broadened to 1 GHz at room temperature, due to Doppler broadening as described in [28]. Thus, the tuning is more permissible that what one can imagine *a priori*. In order to conserve the coherence of the medium, one shall minimise the decay rate by minimising the interaction with the atomic medium. The main source of interaction being the collision between atoms and the cell's wall, a buffer gas is used to slow down the atoms and thus increase the coherence time of the medium.

3.2.2 Atomic probing

The atomic medium being polarised, it acts now as a magnetic dipole. Such a dipole will interact with a magnetic field, this is what will be probed.

In free-induction-decay, the medium is pumped alternatively, in between those pumping steps, one observe through the transmitted polarisation of a linearly polarised beam, the Larmor precession of the atomic magnetic dipole, *e.g.* coherent atomic spin. This leads us to the Bloch equation:

$$\dot{\mathbf{M}} = -\mathbf{M} \times \mathbf{B} + \Gamma \begin{pmatrix} -M_x \\ -M_y \\ M_a - M_z \end{pmatrix} \quad (10)$$

Given that, $\Omega_{\mathbf{L}} = \gamma \mathbf{B}$ the vectorial Larmor frequency, one can retrieve the precession alongside with the pumping effect in this Bloch equation. Linearly polarised beam will thus interact differently according to the global magnetisation. And one can access the orthogonal or the coaxial (to the pump beam) magnetic field component reading respectively the magnetic resonance [16] or the non-linear magneto-optical rotation (*Faraday rotation*) using a balanced detection [29].

4 Implementation

This section is intended to describe the set-up that has been used. One of the final and most detailed configuration of the global set-up is depicted in appendix A. Main scientific results are postponed to section 5.

4.1 852nm Laser source

The source that is at my disposal during this study is a 850nm tunable ECDL (TEC-850-20 from Sacher-lasertechnik) in a Littman-Metcalf configuration of type I (see section 3.1, figure 2) that is combined with a MLD 1000 driver. This tunable ECD was used for the last-known time approximately 25 years ago and remained untouched since that time. Hence the documentation of this Laser set-up is not available and we have little to no specifications (only [30]). We suspect this ECDL to be not containing the original Laser Diode but have no piece of information on this new one. We thus decided to use a maximum current of 130 mA and a working current from 65 mA to 125 mA considering the last know settings used.

Moreover, during my internship we worked especially on the ECDL aiming at repairing and fine-tuning it. This work focused on two aspects: the tuning and cooling systems. One primordial aspect of this configuration is within the tuning-system. The mirror is supported by a flexure which is pushed by a piezo-electric compound. After the first injection in the Fabry-Perot cavity (see section 4.3), the piezo appeared to be dying. Indeed, it stopped answering our scanning ramp after a few minutes. After through-full investigations, we confirm that the piezo-electric needed to be changed. As a proof of principle, we replaced the old 40 mm piezo-electric with a new one, much shorter adapted through a 3D-printed support (see appendix B, figure 23).

4.2 Shape, power of the LASER source

The question of the shape of the LASER source is central to process the beam and to pump/probe effectively the atomic cell. Indeed, having a gaussian-like shaped LASER beam is essential for the fibre coupling. Futhermore, the overall manipulation of such a beam is much easier.

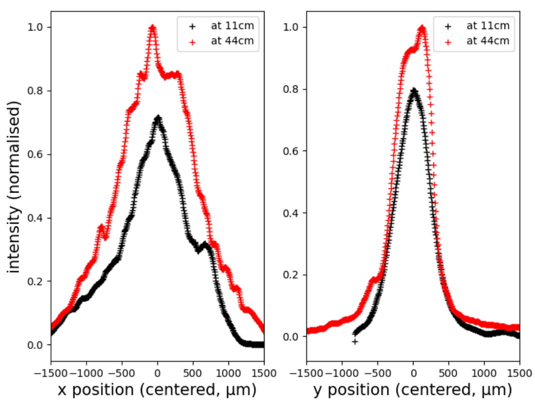

Figure 3: Raw beam's vertical (right) and horizontal (left) sections. Intensity profile of the beam at 11 cm and 44 cm of the source.

The shape of a LASER beam is measured using a camera. During such a measurement, one should be interested in comparing the waist of the beam in two orthogonal directions in the longitudinal plan in respect to the propagation direction.

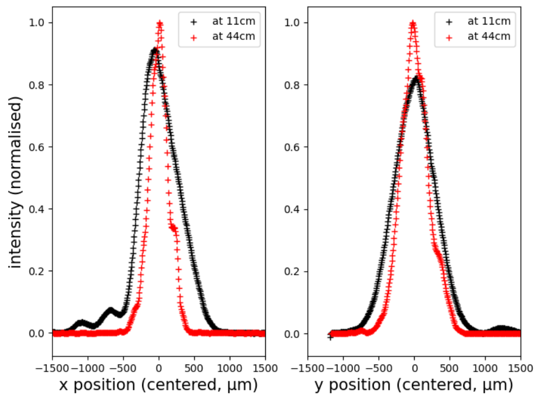

Figure 4: Corrected beam's vertical (right) and horizontal (left) sections. Intensity profile of the beam at 11cm and 44cm of the source.

The waist of a gaussian beam being given by:

$$w(z) = \frac{\text{FWHM}(z)}{\sqrt{2\ln(2)}} \tag{11}$$

and the full width at half maximum being driven by:

$$FWHM(z) = 2\sqrt{2\ln(2)}\sigma(z) \tag{12}$$

where σ is the standard deviation of the Gaussian beam model and z is the distance from the LASER source (according to [31]). Hence $w(z) = 2\sigma(z)$. After a numerical fit, we found a waist of 1 156 µm along U direction and 521 µm along V direction at 44 cm of the LASER source. This waist is comparable with the waist at 11 cm (1 033 µm and 507 µm) from the LASER source. This beam needs to be corrected hence the use of a corrective prism assemble with an aspect ratio of 3.5. After correction, the measurement of the waist is depicted in figure 4.

The final shape of the corrected beam right before the Cs cell is depicted in figure 5. It has been considered sufficient for our application.

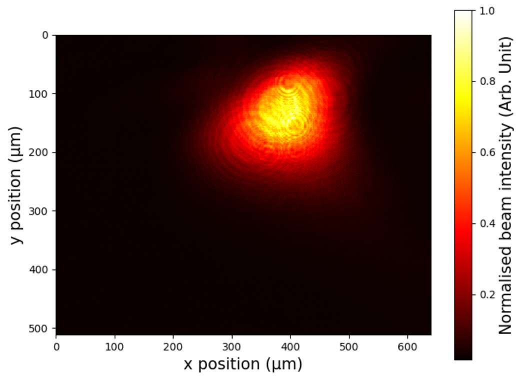

Figure 5: Corrected beam's shape right in front of the Cs cell. Beam intensity is normalised. The beam diameter throught the cell is of 2 mm even though on this picture, the beam appear to be much smaller due to attenuation.

The beam power at the exit of the LASER source is of maximum 17,5 mW. The transmitted power to the Cs cell ranges from 1,2 mW to 3,4 mW.

4.2.1 Tuning

Such a repair implied the disassembly of the mirror support, hence the (re)-alignment of the LASER cavity. This can be done in three steps: (1) Align the first diffraction order of the grating with the tuning mirror vertically using the piezo tuning screw ; (2) Align this same first order laterally using the grating flexure ; (3) Fine tune this lateral alignment. This last step can be done using the minimisation of the LASER threshold as an indicator of the cavity lateral alignment's quality. Using a beam viewer[3] one can determine the LASER threshold as depicted in figure 6. When going past the threshold, the LASER power will suddenly evolve much faster. Exactly at the threshold, the beam will be flashing by quickly starting and stopping to lase. In order to optimise this threshold, one places themselves right under the current threshold and adjust the grating flexure until one sees the beam lasing again. At this point, we lower the current and adjust again. Starting at a threshold of approximately 90 mA, we repeated those steps until we found an optimum at 46 mA which is the same order of magnitude as in equivalent set-up (such as LD-0860-0080-AR-3 from Toptica). This threshold have been measured and optimised to that value frequently as it is an indicator of the LASER cavity alignment's quality.

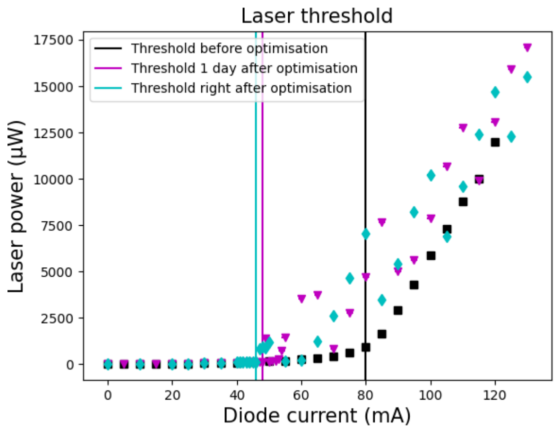

Figure 6: The LASER thresholds evolution with respect to cavity alignment.

4.2.2 Cooling system

A LASER wavelength and quality being very dependant to the diode and cavity temperature, a cooling/heating system is needed. The MLD 1000 temperature control stopped to function not long after the piezo-electric system has been changed and adjusted. This led to further delay in the implementation but an improvement of the temperature control's quality (now on called TEC quality). The TEC is composed of a Peltier module, a current Proportional Integrator/Derivator (PID) servo controller and a

[3] We are indeed working with a near infrared (NIR) LASER , meaning the beam is not visible. A beam viewer is an active tool that convert IR light in visible light. A revealing card can also be used for easier process and both solution have been put in place.

temperature probe.

Not knowing the type of temperature probe that was implemented before in the ECDL, the probe have been changed to a 10 kΩ thermistor, the Peltier module remained unchanged and a seperate current controller have been put in place of the integrated one in the MLD1000. This led to an extension of the TEC range[4]. The temperature/wavelength relationship is linear in such a case, the slope have been measured to 0,13 nm K^{-1} which is, once again, conform to the expectation of such a slope value at this wavelength. Such a fact was not surprising and already measured in the literature [32].

4.3 LASER analysis

The analysis of the LASER wavelength and quality have been done through a wave-meter (WaveMaster from coherent [33]) and a Fabry-Pérot cavity (used in [34]). Those being remote from the optical table where the set-up was supposed to be implemented, optical fibres have been used (see appendix D for more details on optical fibres, beam injection).

On the Wave-meter beam, a optical density (O.D. 4.0) has been used, *e.g.* the beam's intensity have been lowered by 10 000 times. In fact, the wave-meter is able to measure from an optical power of a few nW hence the need of a power reducer, because the only propriety of the beam used here is its frequency. A multi-mode optical fibre has been implemented to transmit the beam from the optical table to the wave-meter, see figure 21 "Towards Wave-meter" in appendix A.

To feed the Fabry-Pérot cavity, a polarisation maintaining optical fibre have been implemented. This is done with a polarisation maintaining single mode fibre with a half wave plate at its enter. The idea of such a set-up is to align the polarisation of the beam with one of the slow/fast axis of the optical fibre, thus maintaining the polarisation independent of the external perturbations. Each Fabry-Pérot peaks are separated by 250 MHz in a $\frac{C}{4L}$ configuration. See figure 21 "Towards Fabry-Pérot Cavity" in appendix A for more details on this part of the set-up and [34].

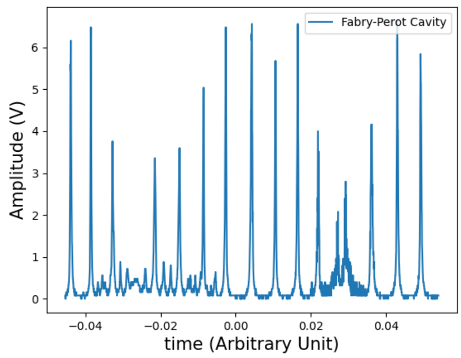

Figure 7: Fabry-Pérot spectrum obtained throught the scan of the piezo-electrical tuning and after the visualisation on a oscilloscope. The time-frequency conversion is now on deduce using the free spectral range (FSR) of the cavity. Two peaks are separated by 250 MHz and a few ms to µs. One can thus refer oneself to the Fabry-Pérot spectrum to measure frequency difference.

4.4 Wavelength and modal purity

Chromatic and modal purity are needed in order to adress efficiently the atomic $\mathcal{D}_2$ transition of Cs . Chromatic first tuning is assured by the adjustment of the piezo device's position. The LASER frequency is then monitored using the wave-meter.

The LASER modal aspect is analysed through the Fabry-Pérot cavity. We considered the piezo to be tuned when the LASER mode hop-free ranges are on both side of the targeted frequency. Temperature, fine-tuning of the piezo and current allows us to shift those mode hop-free ranges on the targeted frequency. Thus, one can access a spectrum such as depicted in figure 7 while scanning the piezo.

[4] We went from an effective range (20 °C to 30 °C) to the range (20 °C to 40 °C), both being limited by condensation (lower limit) and Diode specification (higher limit).

In this figure 7, the spectrum is divided in three zone. In two of those three, the spaces between Fabry-Pérot peaks are noisy, with eventually secondary peaks. On figure 7 these zones are from $-0{,}04$ A U to $-0{,}005$ A U and 0,02 A U to 0,04 A U . Those area are multi-modal functioning-area of the LASER . In between, one can see 4 alone peaks that are characteristic of the single mode regime. For reference, each peaks are separated by 250 MHz, which means the mode hop-free range is approximately of 1 GHz. By fine-tuning the LASER cavity alignment, one can enhance the single mode area and make it larger such as in figure 14.

4.5 Cs Absorption

One of the main step toward Cs magnetometry is being able to probe the Cs hence to perform an absorption spectrum[5]. To do so, and because next steps will use this same system, we decided to implement a home-made balanced detection using balanced photo diodes. This system is depicted in figure 8. This aims at subtracting a reference to the spectroscopic signal in order to ignore the fluctuations of the LASER power.

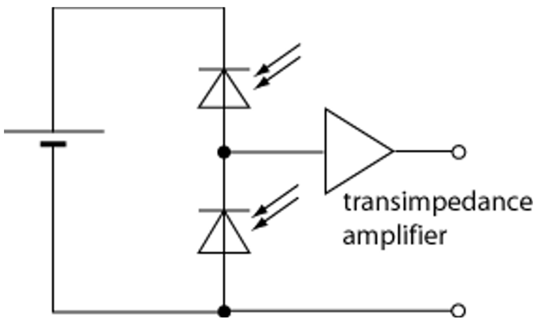

Figure 8: One possible implementation of a balanced photo-detection using two photo diodes.

Flip mirrors have been implemented to be able to switch between the absorption spectroscopy set-up and the magnetometry set-up. The beam have been enlarged by two times in order to interact with more atoms on its path at the saturation intensity.

4.6 Atomic pumping and probing

Atomic pumping in ensured by a left-circularly polarised beam by a Quarter Wave Plate. Because pumping may have to be interrupted depending on the technics that is chosen, a 110 MHz Acousto-Optic Modulator (AOM) has been implemented. This device is using a crystal in which an acoustic wave is being propagated transversally to the beam's direction. This wave is generated by a piezoelectric device driven by a RF generator at 110 MHz and a amplifier delivering 2 W of power as specified in the documentation of the AOM. This AOM is inducing a frequency shift of 110 MHz of the LASER and an angular deviation of the first order of refraction. This first order is then selected through an iris, by doing so, the pumping beam is only entering the cell when the AOM is on. We thus successfully created an electronic shutter, with an response time in the order of magnitude of the nanosecond.

Atomic probing can be accomplished using a separated beam, linearly polarised. This is to probe a *Faraday rotation* through the Cs medium. Such a probe is extended radially to ensure that all the polarised atoms are interrogated. Moreover, it is very important that the two contra-propagating beams are overlap in order to pump and probe the same atoms. Thus a special attention has been paid during the alignment of this set-up. In order to extract the information from that probe beam, 10% of its power is extracted using a 10/90 beam splitter (BSF-10-B from Thorlabs [35]). In order to have no or little impact on the beams polarisation, one needs to pay attention to the angular orientation of such a device. Furthermore, the back of this device is made to be specifically non reflective (see figure 9). From the specifications (see figure 10), we could establish that down from 25°, the polarisation maintaining is sufficient for our use case.

[5]Indeed, we need to lock our LASER frequency around a specific Cs transition.

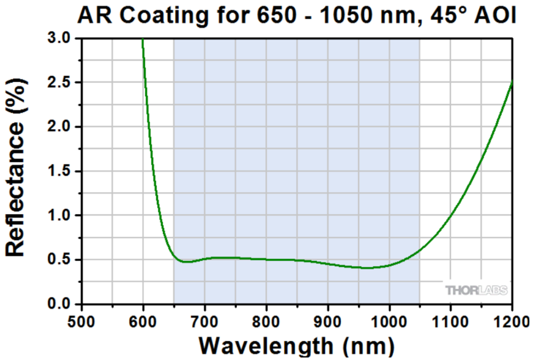

Figure 9: Reflected power on the back face of the beam splitter according to [35]

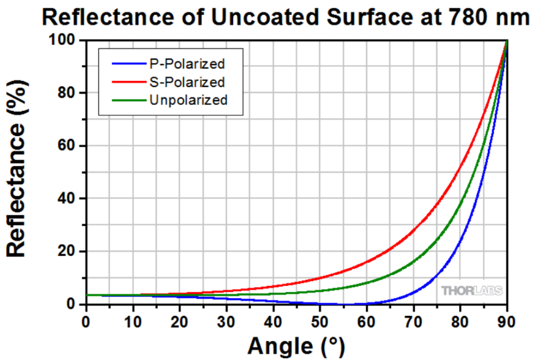

Figure 10: Reflected beam's polarisation at 780 nm according to [35]

The final step is to extract the information from the probe beam. To do so, we used the balanced photo-diodes set-up combined with a half wave plate and a polariser beam splitter. Thus one can separate the horizontal and vertical polarisation from the beam and then plot the rotation of the polarisation, that is what we want to do.

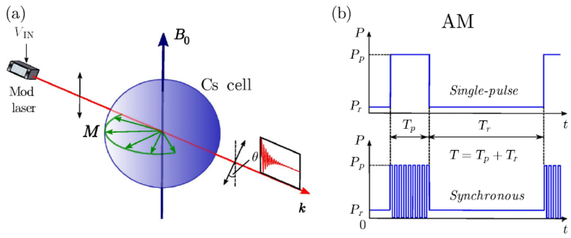

Figure 11: In the Cs gas, all the atoms have aligned spin (through pumping) creating a collective spin. This state is later called polarised state. In the Free induction decay method, we polarise the Cs orthogonally to the magnetic field. The collective spin will then turn following Larmor mechanism. This medium is birefringent and a linearly polarised probing beam will have its polarisation turned. Figure extracted and cropped from [17].

5 Measurement

5.1 Cs cell characterisation

The next step toward magnetometry is the realisation of the Cs cell abortion spectrum and their proper characterisation. A Cs cell is a glass-work having low pressure or vacuum conditions and solid Cs. Cesium vapour is produced through the equilibrium vapour pressure (saturated vapour pressure) of the solid cesium. We have at our disposal more than 20 years old spectroscopic Cs cell that are $l = 5$cm, $d = 3$cm cylinders, two $1 \times 1 \times 1$cm cubes with 50 torr and two of the same shape with 150 torr of N_2 buffer gas. Those cells are uncoated but have 2 (for the old cell) and 4 optical surfaces (for the new cell). Some pictures of those cells are in figures 12 and 13.

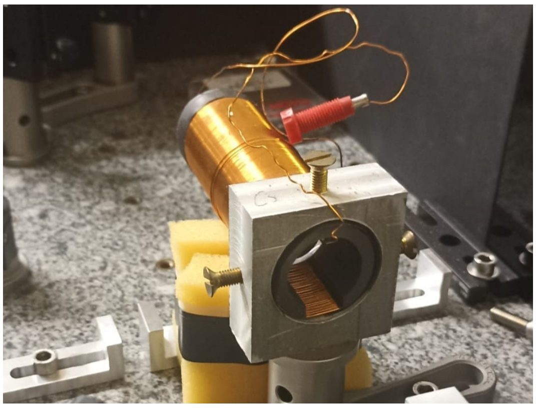

Figure 12: The old spectroscopic cell with its surrounding coil used to generate magnetic field.

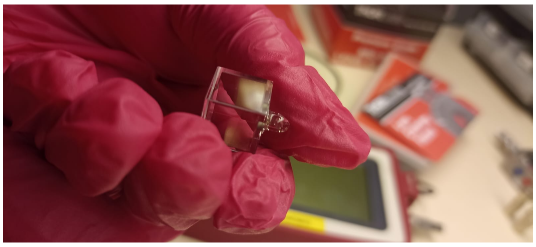

Figure 13: One of the new cell after the heating and desorption process. We can clearly see the presence of a solid on all the walls of the cell.

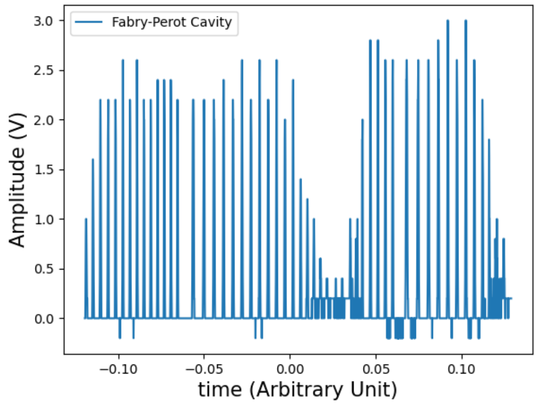

Figure 14: Much larger hop-free range of around 3,75 GHz. This is the condition in which the spectrum of the Cs cell has been for the first time established in our experiment. One can see that their is a hop between two single mode area. In that case, counting the peaks does not provide a good estimation of the frequency scan through this hop.

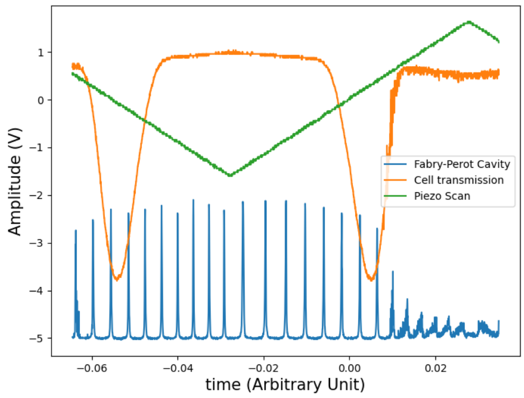

Figure 15: In this figure, a scanning ramp is corresponding to a piezo scan of 3 GHz.

We started by establishing that the theoretical transmission rate of such cell should be approximately 84.9%. Indeed, there is 4 glass-air/gas interfaces that have each a 4% loss rate, hence $0.96^4 = 84.9\%$ of transmission rate. Such transmission rate have been reached on the spectroscopic cell. On the new cells, the transmission rate was both fluctuating between the same specification cell and low (between 49% and 56%). This is explained by the fact that a solid was coating partially the optical surfaces. Nonetheless, this rate is sufficient for a first absorption spectrum.

The absorption spectrum of the spectroscopic cell was established (see figure 15) around the $\mathcal{D}_2$ transition. Thanks to a hop in the scanning, we could establish the whole $\mathcal{D}_2$ transition spectrum (including the hyperfine splitting of 9 GHz). This is depicted in figure 16. The splitting size have been confirmed by the wave-meter. Moreover, it is centered on the theoretical value of 852,347 nm.

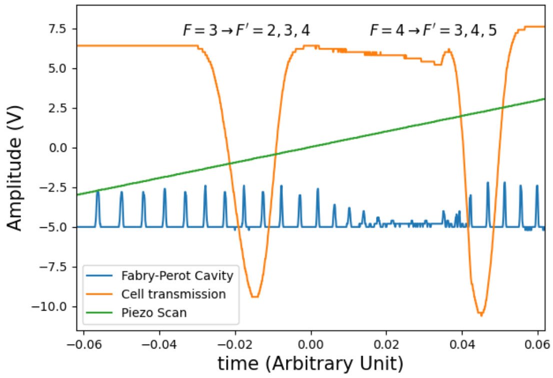

Figure 16: Depiction of the $\mathcal{D}_2$ transition with the hyperfine split of 9 GHz enabled by the hop between to single-mode. The excited hyperfine levels are combined in the same peak because they are separated of 151,21 MHz to 251,00 MHz which is negligible compared to the 9 GHz hyperfine splitting [28].

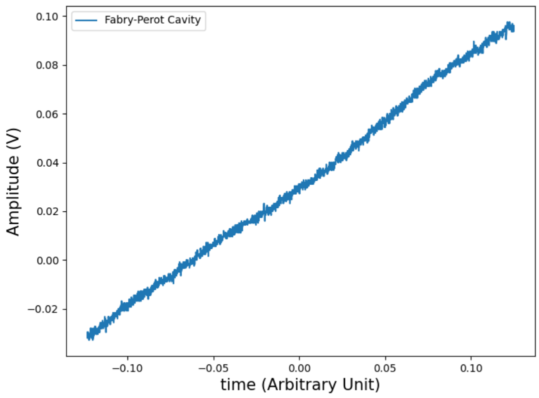

Figure 17: Not heated cell with a small signal of a few mV.

The evaluation of the new cell leads to the implementation of a secondary spectrograph set up. This enables us to superpose both spectrum for comparison. Little to no traces of Cs has been observed on this first spectrum. According to [28], a 1 GHz pressure shift could explain that fact. After thorough research of the spectrum, we found that the Cs cell have a little spectroscopic signal as depicted in figure 17.

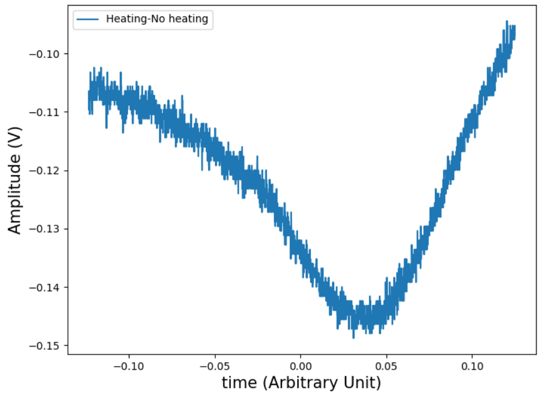

Figure 18: The difference between heated and not heated 50 torr cell produce this signal.

To enhance the signal, we decided to heat the cell and take the difference as plotted in figure 18.

If a signal is definitely here, one can see that it is some order of magnitude smaller than the one coming from the spectroscopic cell (approximately 100 times smaller). We concluded that this is the result of a lack of cesium in those untested cell. We made the hypothesis that a reaction between the buffer gas (nitrogen) and Cs could have happened during the one year storage before my internship. However, even if some chemistry exercises suggest such a reaction, several teams using those type of cell reported no alteration of the cell after a long storage. We therefore could not conclude on this lack of Cs this way. According an estimation of Benjamin Pasquiou[6] the pressure broadening and the difference of length of the cell are not enough to explain that ratio of amplitude. Despite all efforts, an unexplained factor 4 remained in the ratio between our two measure-

[6] Benjamin Pasquiou is a CNRS research engineer in the Chromium team.

ment. Further investigation needs to be done on this subject.

The desorption of the Cs from the pyrex cell's wall has been tried using a 405 nm LASER diode with around 20 mW of power. This resulted in no amelioration of the signal.

5.2 Magnetic field measurement

5.2.1 Parameters of the experiment and chosen set up

Due to a lack of time we implemented the method that appeared to be the easiest in our configuration: the Nonlinear Magneto-Optical Rotation (NMOR). The pumping and probing beam can be the same in this technic [29]. That is what we did using the probing as both probing and pumping circularly polarised. We modulate the frequency of the LASER at Ω_m taking values from 250 MHz to 1 000 MHz. The magnetic field is generated with a coaxial coil with respect to the probing/pumping beam and scanned through a current source driven by a function generator generating a ramp at frequency from 100 mHz to 100 µHz.

An unbalanced detection is demodulated using a moku-go ([36]) in lock-in configuration. The inputs are the sinusoidal Ω_m modulation and the unbalanced detection. Considering the frequency of modulation, we use a photo-diode with variable gain and a response time under the µs at 20 dB. Due to the absence of documentation, we suppose that the connexion is through a T-connector which acts as a low-pass filter and a SMA port. In order to keep a clean modulation signal, we avoid any high frequency harmonic, hence the use of sinusoidal modulation in current. As 10 V corresponding to 3 A, we have a converting ration of $k = 0{,}3$ A mV^{-1}. Placing ourselves at the center of the coil, considering the length of the cell (5 cm) being small compared to the length (10 cm and with R =1,5 cm the cell radius, $n = \frac{100}{0.6} = 166$ the number of turns, I the intensity, U the driving tension of the function generator, μ_0 the magnetic field constant, the Biot-Savart's law gives:

$$B = \frac{\mu_0 n I}{2R} = \frac{\mu_0 n U k}{2R} \tag{13}$$

This law has been used to compute the magnetic field created by the coil. We shall keep in mind the influence of the earth's magnetic field in our interpretation. Indeed, the cell is oriented in the North-South direction. The different results are presented in page 16.

5.2.2 Interpretation

Those results are difficult to interpret and further exploration needs to be done. However we managed to extract some possible explanations and interpretations. Before making any statement, we shall notice that this experimentation is very sensible to the LASER tuning and mode. We had to compensate for the LASER shift several times throughout this experimentation and exit the multi-mode emission areas. Firstly figures 19a and 19b depict the same experiment conducted several times. Indeed, the stability of the signal was not established at first, and we decided to conduct the same experiment several times in order to identify what structures are physically related signal. We especially paid attention to the dispersive signal that should be seen according to [29]. Although we established the signal presented in those figures is repeating, its asymmetry combined with its instability leads us to further investigations. Therefore, we focused on the symmetrical part of this signal which was the near-zero part (dips occurring symmetrically and repeatedly).

In fact, the next step consisted in changing the current source to a bipolar current source. Indeed the dips suggested in the last paragraphs seemed to occur in a near-zero field. We thus investigated the zero-crossing field situation. This is a situation where we need to take into account the presence of the earth's magnetic field shift the zero of the magnetic field in one or another direction. This has been done in figures 19c and 19d. A highly symmetrical signal is achieved in 19d while 19c demonstrate the instability of the signal in general and more especially in the first few periods of the magnetic scan. Moreover, we can observe the presence of the near-zero dip describe and suggested in figures 19a and 19b.

We decided to invert the direction of the generated magnetic field. This has been done through the inversion of the polarisation of the current source. This is the only difference between figure 19c and 19d. We can clearly establish the inversion of the dispersive signal between those two figures with respect to the magnetic field value. In addition to that, the dip is situated at 35 mV off compared to zero. When inverting the direction of the generated magnetic field, the dip is situated at -80 mV. This leads to a 0,47 G magnetic field. The International Geomagnetic Reference Field (IGRF) simulator is estimating the horizontal N-S magnetic field to be of approximately 0,315 G. Considering the important errors that reside in the reading of such values, this measure is compatible with the measurement of the earth magnetic field by 19,75 %.

In order to have a stronger proof of the polarisation inversion's impact, even though the signal can be unstable, we decided to do the inversion through the scan. This is what have been done in figure 20a. We can see that the signal is been repeated which is a strong proof of the magnetic field observation.

Finally, we decided to explore the demodulation frequency's impact. Figures 20b to 20d show such an impact. Even thought the interpretation of those data is difficult, we can observe that the higher the demodulation frequency is, the more details we have in the demodulated signal. Moreover, the near-zero magnetic field dip is present throughout all the signals and the same global structure is respected. Two peaks are present in all the configuration. The two times slower scan of the magnetic field seems also to have increase the amount of information that one can extract. The global signature of a dispersive signal is well conserved while changing the demodulation frequency.

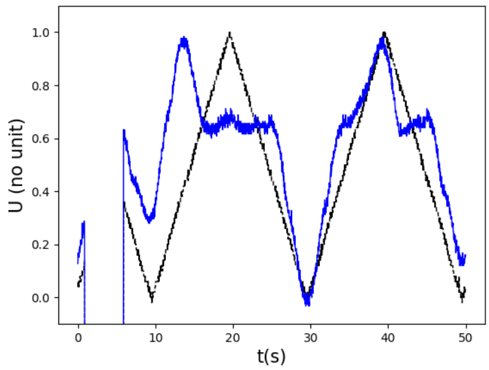

(a) Demodulation at 750 kHz. The magnetic field is scanned from 0 G to 4,17 G at 2 Hz.

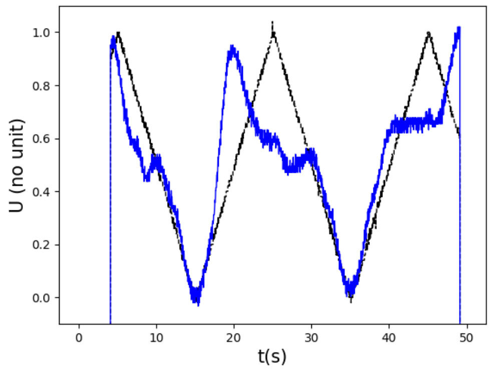

(b) Demodulation at 750 kHz. The magnetic field is scanned from 0 G to 4,17 G at 2 Hz.

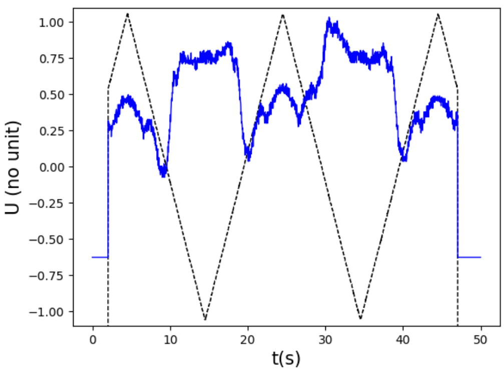

(c) Demodulation at 1 MHz. The magnetic field is scanned from 0 G to 16,368 G at 2 Hz.

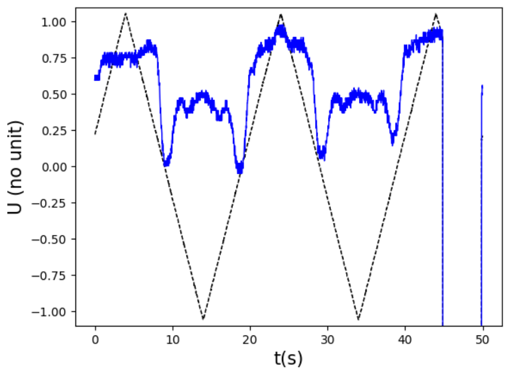

(d) Polarity inverted compared to 19c. Demodulation at 1 MHz. The magnetic field is scanned from 0 G to 16,368 G at 2 Hz.

Figure 19: First qualitative test of magnetometry. Every measure has been done with a scan of the magnetic field at 2 Hz. Blue trace is the demodulation of the photo-diode, the black trace is the magnetic field scan. An independent normalisation has been applied on each of those traces. The physical information laying within the dynamic of the demodulated signal with respect to the magnetic scan.

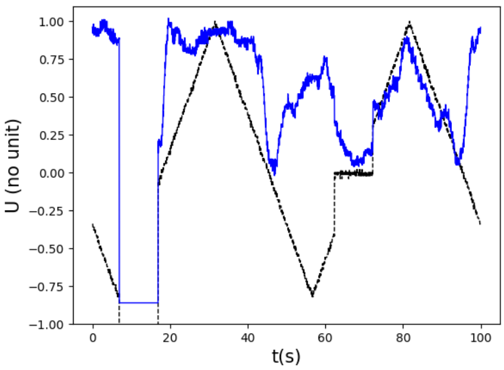

(a) Polarity inversion of the magnetic field at 65 s to 75 s done mannualy by inverting the connexion between the current generator and the coil. Scan from −16,368 G to 20,86 G.

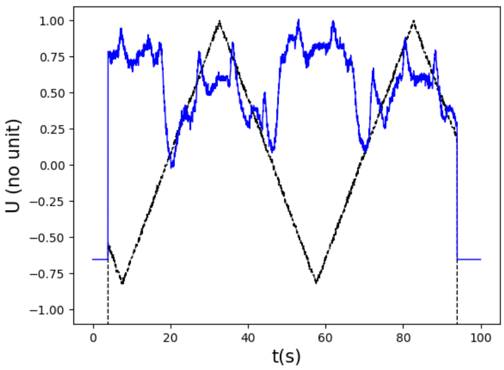

(b) Demodulation at 1 MHz. Scan from −16,368 G to 20,86 G.

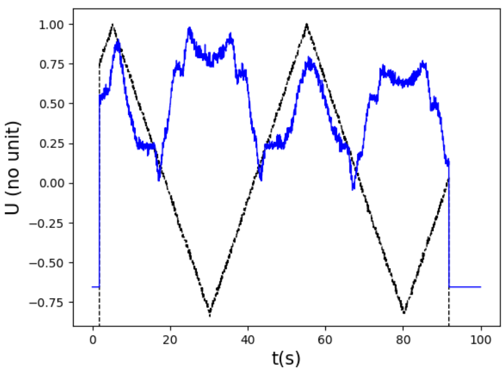

(c) Demodulation at 500 kHz. Scan from −16,368 G to 20,86 G.

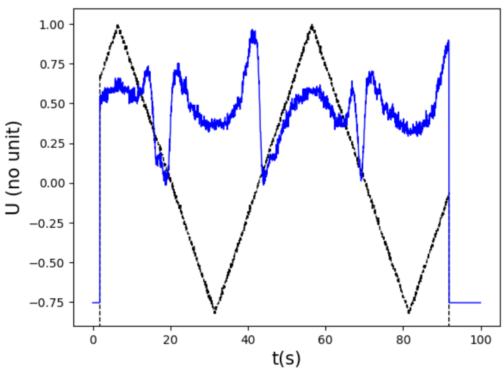

(d) Demodulation at 250 kHz. Scan from −16,368 G to 20,86 G.

Figure 20: Different frequency of modulation/demodulation in 20b to 20d and polarity inversion of the magnetic field in 20a. Every scan is at 1 Hz.

6 Conclusion and perspectives

In order to conclude, we successfully managed to repair and fine-tune the 25-year old 852 nm LASER. However, this LASER is not stable and we identify two major issues. First is its shifting tendency. This experiment's Signal-Noise Ratio (SNR) is greatly impacted by placing ourselves in the center of one of the two hyperfine $\mathcal{D}_2$ transition. Second is the fact that the LASER needs to be single-mode. If it is not the case, the SNR is tremendously unusable.

We then established that the new Cs cell ordered for this experimentation are far from being usable, even after a desorption manipulation or a heating. Even though the heating produced some amelioration that could be exploited, the final cell being placed in ultra-vacuum, this add too much complexity to the experiment. New Cs cell should be ordered after the absence of the Cs has been explained. We also demonstrated that the spectroscopic cell, with no buffer gas is still usable. The buffer gas being essential to have a exploitable coherent time, this cell cannot be used for FID in the vacuum.

Finally, a proof of concept of magnetometry has been established. Even thought the final application in the Chromium experimentation will be using the Free-Induction Decay (FID) method, the Non-linear Magneto Optical Rotation (NMOR) method has been successfully implemented. NMOR has been successfully achieved with less means than what has been founded in the literature, using unbalanced detection. This work is thus a proof of concept of magnetometry and opens the way for the Chromium team to explore further the atomic magnetometry. Further investigation of this set up are needed in order to fully understand the magnetic field detection, especially concerning non-zero magnetic-fields and the demodulation frequency impact on the measurement.

References

[1] Bose. "Plancks Gesetz und Lichtquantenhypothese". In: *Zeitschrift für Physik* 26.1 (Dec. 1, 1924), pp. 178–181. ISSN: 0044-3328. DOI: 10.1007/BF01327326. URL: https://doi.org/10.1007/BF01327326 (visited on 06/08/2026).

[2] F. London. "The Lambda-Phenomenon of Liquid Helium and the Bose-Einstein Degeneracy". In: *Nature* 141.3571 (Apr. 1938), pp. 643–644. ISSN: 1476-4687. DOI: 10.1038/141643a0. URL: https://www.nature.com/articles/141643a0 (visited on 06/08/2026).

[3] M. H. Anderson et al. "Observation of Bose-Einstein Condensation in a Dilute Atomic Vapor". In: *Science* 269.5221 (1995), pp. 198–201. ISSN: 0036-8075. JSTOR: 2888436. URL: https://www.jstor.org/stable/2888436 (visited on 06/10/2026).

[4] K. B. Davis et al. "Bose-Einstein Condensation in a Gas of Sodium Atoms". In: *Physical Review Letters* 75.22 (Nov. 27, 1995), pp. 3969–3973. DOI: 10.1103/PhysRevLett.75.3969. URL: https://link.aps.org/doi/10.1103/PhysRevLett.75.3969 (visited on 07/16/2026).

[5] Q. Beaufils et al. "All-Optical Production of Chromium Bose-Einstein Condensates". In: *Physical Review A* 77.6 (June 2, 2008), p. 061601. DOI: 10.1103/PhysRevA.77.061601. URL: https://link.aps.org/doi/10.1103/PhysRevA.77.061601 (visited on 06/08/2026).

[6] Axel Griesmaier. "Bose-Einstein Condensation of Chromium". In: *Physical Review Letters* 94.16 (2005). DOI: 10.1103/PhysRevLett.94.160401.

[7] Lucas Gabardos et al. "Relaxation of the Collective Magnetization of a Dense 3D Array of Interacting Dipolar $S=3$ Atoms". In: *Physical Review Letters* 125.14 (Sept. 30, 2020), p. 143401. DOI: 10.1103/PhysRevLett.125.143401.

URL: https://link.aps.org/doi/10.1103/PhysRevLett.125.143401 (visited on 07/24/2026).

[8] Youssef Aziz Alaoui et al. "Measuring Correlations from the Collective Spin Fluctuations of a Large Ensemble of Lattice-Trapped Dipolar Spin-3 Atoms". In: *Physical Review Letters* 129.2 (July 6, 2022), p. 023401. DOI: 10.1103/PhysRevLett.129.023401. URL: https://link.aps.org/doi/10.1103/PhysRevLett.129.023401 (visited on 07/24/2026).

[9] Youssef Aziz Alaoui et al. "Measuring Bipartite Spin Correlations of Lattice-Trapped Dipolar Atoms". In: *Physical Review Letters* 133.20 (Nov. 13, 2024), p. 203401. DOI: 10.1103/PhysRevLett.133.203401. URL: https://link.aps.org/doi/10.1103/PhysRevLett.133.203401 (visited on 07/24/2026).

[10] Cameron Deans et al. "Electromagnetic Induction Imaging with a Radio-Frequency Atomic Magnetometer". In: *Applied Physics Letters* 108.10 (Mar. 10, 2016), p. 103503. ISSN: 0003-6951. DOI: 10.1063/1.4943659. URL: https://doi.org/10.1063/1.4943659 (visited on 06/10/2026).

[11] Xuanyao Bai et al. "Atomic Magnetometers and Their Application in Industry". In: *Frontiers in Physics* 11 (June 8, 2023). ISSN: 2296-424X. DOI: 10.3389/fphy.2023.1212368. URL: https://www.frontiersin.org/journals/physics/articles/10.3389/fphy.2023.1212368/full (visited on 06/10/2026).

[12] Tim M. Tierney et al. "Optically Pumped Magnetometers: From Quantum Origins to Multi-Channel Magnetoencephalography". In: *NeuroImage* 199 (Oct. 1, 2019), pp. 598–608. ISSN: 1053-8119. DOI: 10.1016/j.neuroimage.2019.05.063. URL: https://www.sciencedirect.com/science/article/pii/S1053811919304550 (visited on 06/10/2026).

[13] Rasmus Zetter, Joonas Iivanainen, and Lauri Parkkonen. "Optical Co-registration of MRI and On-scalp MEG". In: *Scientific Reports* 9.1 (Apr. 2, 2019), p. 5490. ISSN: 2045-2322. DOI: 10.1038/s41598-019-41763-4. URL: https://www.nature.com/articles/s41598-019-41763-4 (visited on 06/10/2026).

[14] Yosuke Ito et al. "Simplified Shielded MEG-MRI Multimodal System with Scalar-Mode Optically Pumped Magnetometers as MEG Sensors". In: *Scientific Reports* 14.1 (Oct. 28, 2024), p. 25867. ISSN: 2045-2322. DOI: 10.1038/s41598-024-77089-z. URL: https://www.nature.com/articles/s41598-024-77089-z (visited on 06/10/2026).

[15] Dominic Hunter et al. "Free-Induction-Decay Magnetic Field Imaging with a Microfabricated Cs Vapor Cell". In: *Optics Express* 31 (Sept. 21, 2023), pp. 33582–33595. DOI: 10.1364/OE.500278.

[16] Anne Fabricant, Irina Novikova, and Georg Bison. "How to Build a Magnetometer with Thermal Atomic Vapor: A Tutorial". In: *New Journal of Physics* 25.2 (Feb. 2023), p. 025001. ISSN: 1367-2630. DOI: 10.1088/1367-2630/acb840. URL: https://doi.org/10.1088/1367-2630/acb840 (visited on 07/07/2026).

[17] D. Hunter et al. "Free-Induction-Decay Magnetometer Based on a Microfabricated Cs Vapor Cell". In: *Physical Review Applied* 10 (July 5, 2018). DOI: 10.1103/PhysRevApplied.10.014002.

[18] William E. Bell and Arnold L. Bloom. "Optically Driven Spin Precession". In: *Physical Review Letters* 6.6 (Mar. 15, 1961), pp. 280–281. DOI: 10.1103/PhysRevLett.6.280. URL: https://link.aps.org/doi/10.1103/PhysRevLett.6.280 (visited on 07/07/2026).

[19] J. C. Allred et al. "High-Sensitivity Atomic Magnetometer Unaffected by Spin-Exchange Relaxation". In: *Physical Review Letters* 89.13 (Sept. 9, 2002), p. 130801. DOI: 10.1103/PhysRevLett.89.130801. URL: https://link.aps.org/doi/10.1103/PhysRevLett.89.130801 (visited on 07/07/2026).

[20] H. C. Huang et al. "Three-Axis Atomic Magnetometer Based on Spin Precession Modulation". In: *Applied Physics Letters* 107.18 (Nov. 2, 2015), p. 182403. ISSN: 0003-6951. DOI: 10.1063/1.4935096. URL: https://doi.org/10.1063/1.4935096 (visited on 07/09/2026).

[21] M. Rosner et al. "A Highly Drift-Stable Atomic Magnetometer for Fundamental Physics Experiments". In: *Applied Physics Letters* 120.16 (Apr. 20, 2022), p. 161102. ISSN: 0003-6951. DOI: 10.1063/5.0083854. URL: https://doi.org/10.1063/5.0083854 (visited on 07/09/2026).

[22] D. Budker et al. "Resonant Nonlinear Magneto-Optical Effects in Atoms". In: *Reviews of Modern Physics* 74.4 (Nov. 20, 2002), pp. 1153–1201. DOI: 10.1103/RevModPhys.74.1153. URL: https://link.aps.org/doi/10.1103/RevModPhys.74.1153 (visited on 07/09/2026).

[23] D. Budker et al. "Sensitive Magnetometry Based on Nonlinear Magneto-Optical Rotation". In: *Physical Review A* 62.4 (Sept. 11, 2000), p. 043403. DOI: 10.1103/PhysRevA.62.043403. URL: https://link.aps.org/doi/10.1103/PhysRevA.62.043403 (visited on 07/09/2026).

[24] Jean-Marc Breguet et al. "Tunable Extended-cavity Diode Laser Based on a Novel Flexure-mechanism". In: *International Journal of Optomechatronics* 7 (July 3, 2013), pp. 181–192. DOI: 10.1080/15599612.2013.807528.

[25] *NIST Optical Frequency Measurements Group*. URL: https://tf.nist.gov/ofm/lasers/ecdls.htm (visited on 07/26/2026).

[26] Wenbo Wang, Arkady Major, and Jitendra Paliwal. "Grating Stabilized External Cavity Diode Lasers for Raman Spectroscopy – A Review". In: *Applied Spectroscopy Reviews* 47 (Feb. 1, 2012). DOI: 10.1080/05704928.2011.631649.

[27] WILLIAM HAPPER. "Optical Pumping". In: *Reviews of Modern Physics* 44.2 (Apr. 1, 1972), pp. 169–249. DOI: 10.1103/RevModPhys.44.169. URL: https://link.aps.org/doi/10.1103/RevModPhys.44.169 (visited on 07/26/2026).

[28] A. Daniel Steck. "Cesium D Line Data". In: *Arkiv* (23 January 1998 (revision 1.6, 14 October 2003)). URL: https://steck.us/alkalidata/cesiumnumbers.1.6.pdf (visited on 07/22/2026).

[29] D. Budker et al. "Nonlinear Magneto-Optical Rotation with Frequency-Modulated Light". In: *Physical Review A* 65.5 (May 2, 2002), p. 055403. DOI: 10.1103/PhysRevA.65.055403. URL: https://link.aps.org/doi/10.1103/PhysRevA.65.055403 (visited on 07/09/2026).

[30] *Wayback Machine*. May 4, 2003. URL: https://web.archive.org/web/20030504100458/http://data.sacher.de/LMN/ln085020.pdf (visited on 07/12/2026).

[31] *Gaussian Beam*. In: *Wikipedia*. July 20, 2026. URL: https://en.wikipedia.org/w/index.php?title=Gaussian_beam&oldid=1365087376 (visited on 07/21/2026).

[32] Yiru Liao et al. "An Experimental Study on the Temperature Characteristic of a 940 Nm Semiconductor Laser Diode". In: *Optics and Photonics Journal* 6.8 (Aug. 25, 2016), pp. 75–82. DOI: 10.4236/opj.2016.68B013. URL: https://www.scirp.net/

journal/paperinformation?paperid=70305 (visited on 07/24/2026).

[33] *Coherent WaveMaster Wavelength Meter - InstrumentHive*. URL: https://www.instrumenthive.com/products/coherent-wavemaster-wavelength-meter/ (visited on 07/26/2026).

[34] Benjamin PASQUIOU. *Excitations of a Dipolar Bose-Einstein Condensate*. Magnetic Quantum Gases. Mar. 28, 2012. URL: https://gqm.lpl.univ-paris13.fr/index.php/2012/03/28/gabriel-bismut/ (visited on 07/17/2026).

[35] *Thorlabs · Beam Samplers*. URL: https://www.thorlabs.com/beam-samplers?pn=BSF10-B&tabName=Graphs (visited on 07/14/2026).

[36] *Moku:Go*. Liquid Instruments. URL: https://liquidinstruments.com/products/hardware-platforms/mokugo/ (visited on 07/26/2026).

[37] *Single-Mode Optical Fiber*. In: *Wikipedia*. July 15, 2026. URL: https://en.wikipedia.org/w/index.php?title=Single-mode_optical_fiber&oldid=1364226622 (visited on 07/26/2026).

[38] *Polarization-Maintaining Optical Fiber*. In: *Wikipedia*. Sept. 27, 2025. URL: https://en.wikipedia.org/w/index.php?title=Polarization-maintaining_optical_fiber&oldid=1313702507 (visited on 07/26/2026).

A Complete set-up

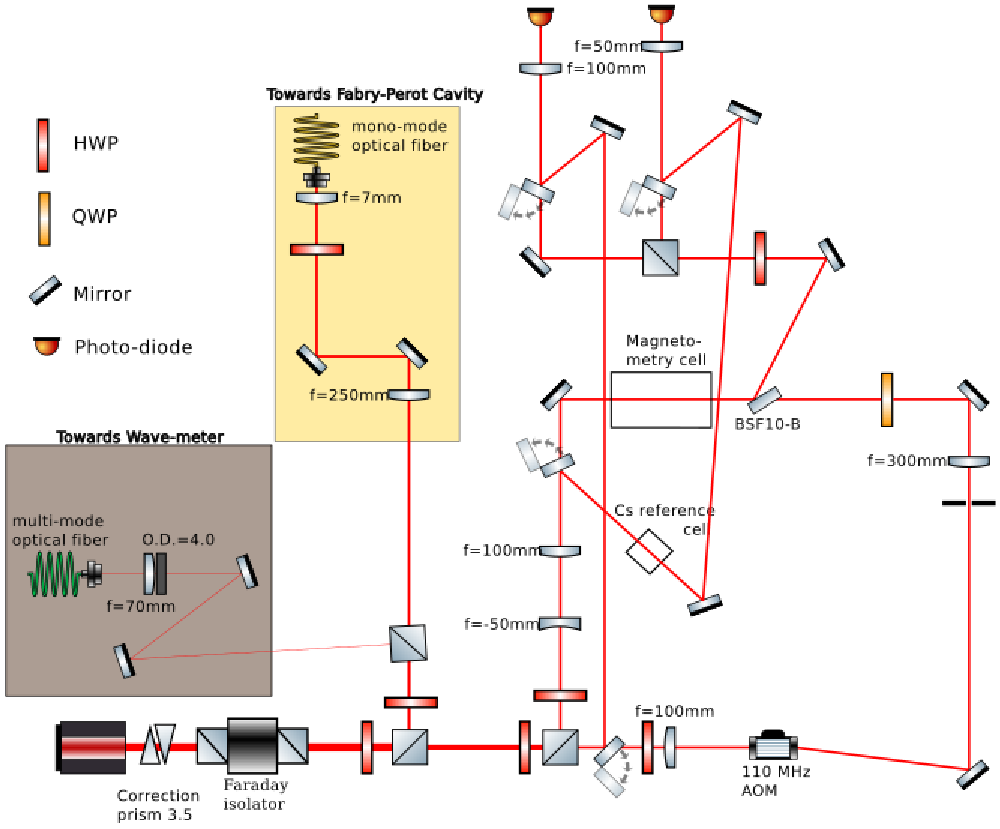

Figure 21: Set-up of the experimentation at its most complete point. HWP: Half Wave Plate, QWP: Quarter Wave Plate, AOM: Accousto-Optic Modulator.

B External Cavity Diode Laser details

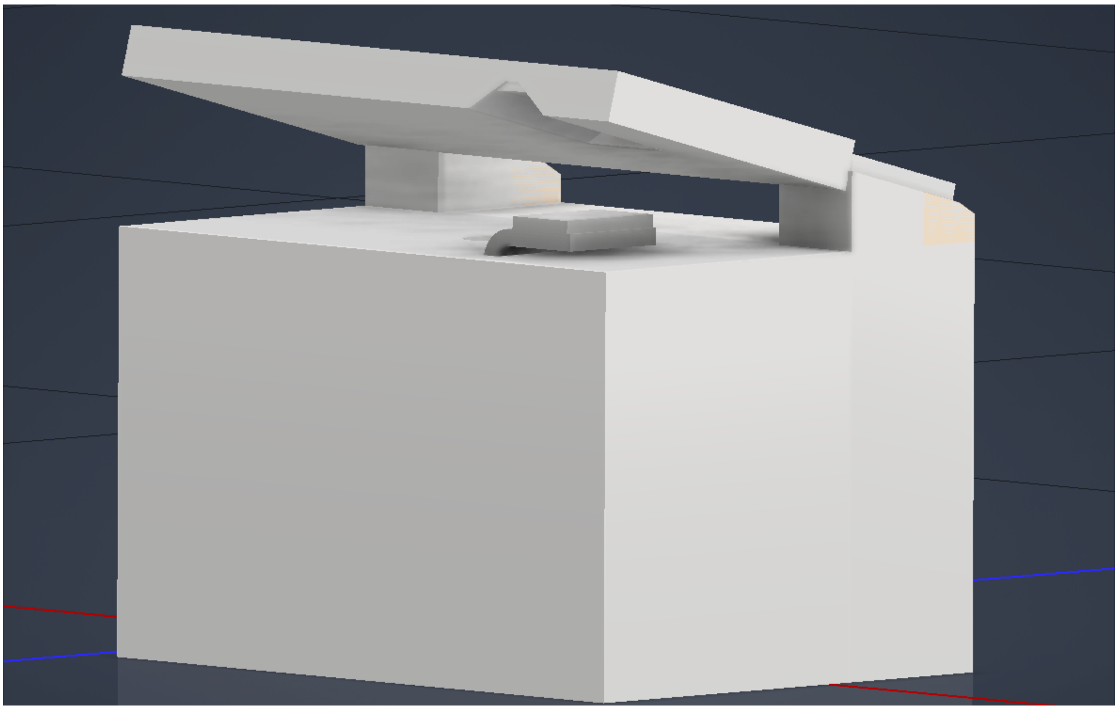

Figure 22: A view of the laser cavity. The diode is at the back of the block, illuminating the grating. This view is for visual representation only and is not exact in proportion neither it is in angles.

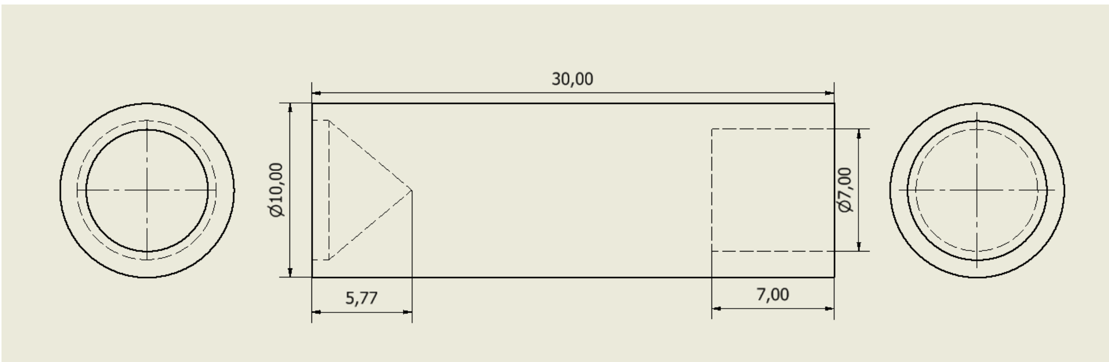

Figure 23: Design of the new 3D printed support that adjusts the new piezo-electric to the system (in the cylindrical hole).

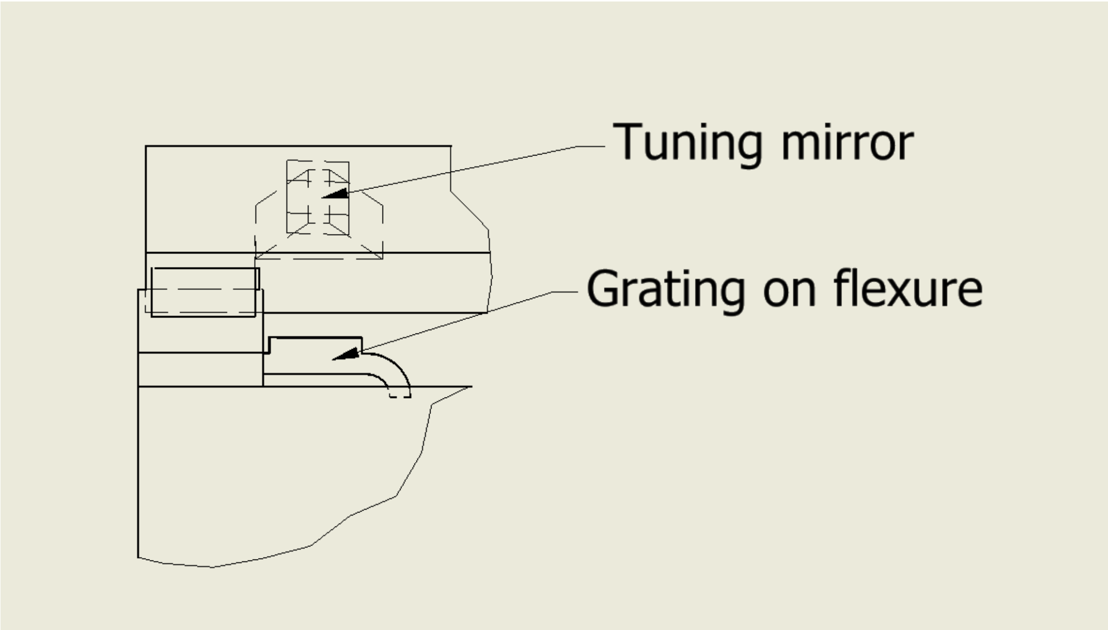

Figure 24: Section of the LASER cavity, the diode is in between the mirror and grating, the grating's flexure is adjusting the lateral alignment of the cavity, the mirror is tuning the laser.

C $\mathcal{D}_2$ transition of cesium

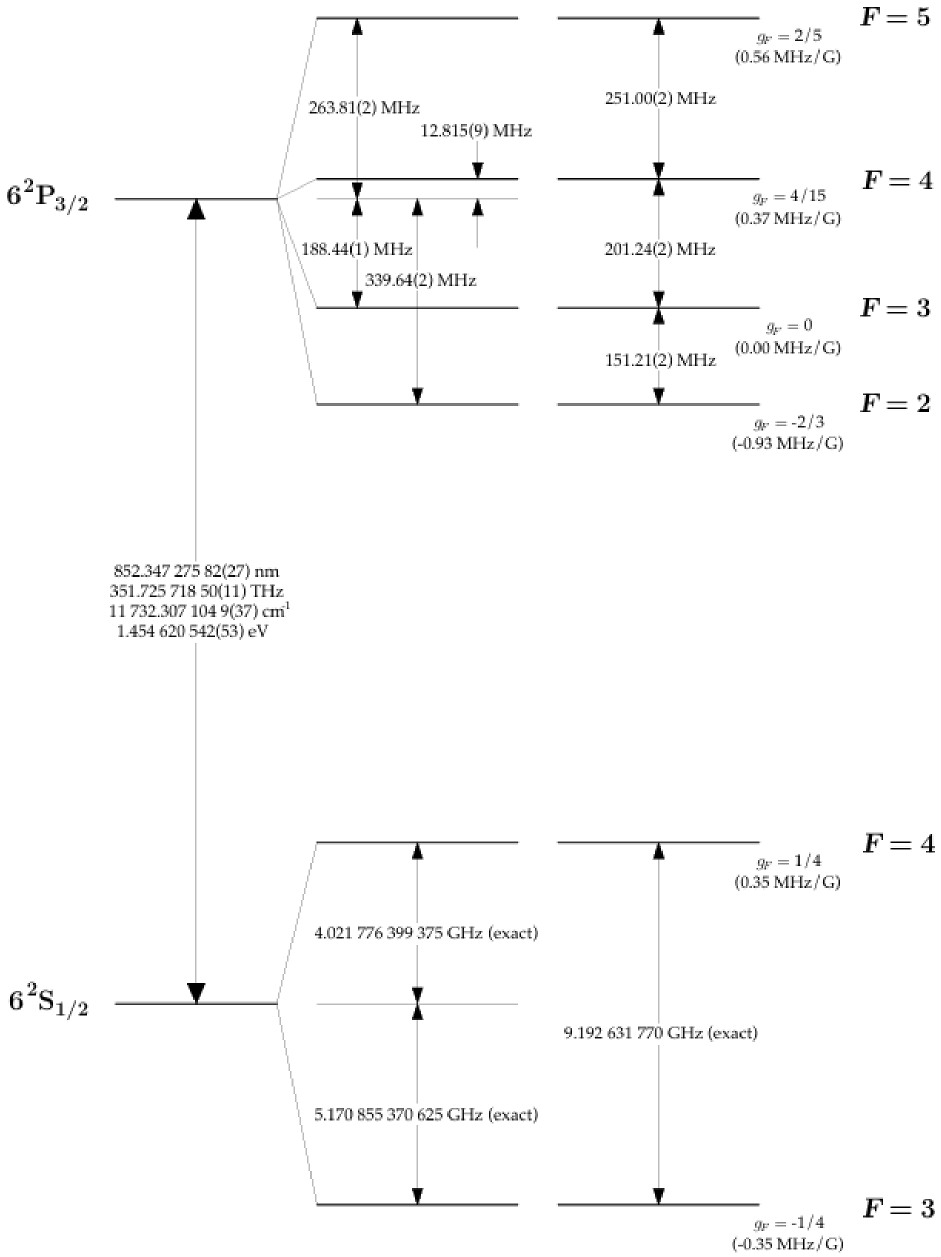

Figure 25: The $\mathcal{D}_2$ transition of cesium. The $F = 3 \to F = 4$ transition in the ground state $6^2S_{1/2}$ is the transition used for the definition of the second [28] We are working around the $F = 3 \to F' \in \{2, 3, 4\}$ and $F = 4 \to F' \in \{3, 4, 5\}$ transition between $6^2S_{1/2}$ (ground) and $6^2P_{3/2}$ (excited) states. Figure extracted from [28].

D Optical fibres

D.1 Concept

Optical fibres are a way of transmitting light through long distance. This is usually done by a onion structure such as in figure 26. The light is propagating through the core.

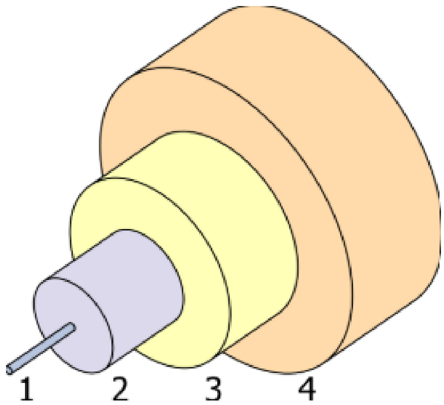

Figure 26: Single-mode fibre typical layout, the core being at most ten times larger than the light wavelength. 1 being the core, 2 the cladding, 3 the buffer and 4 the jacket. From [37].

The propagation is due to total reflection at the interface of the core and the cladding. The core (n_1) and cladding (n_2) refractive index being different ($n_2 < n_1$), a total reflection can occur if the incident light is contained within an acceptance cone define by the critical angle: $\theta_c = \arcsin(n_1/n_2)$.

Being within that acceptance cone is one of the two condition of coupling in an optical fibre. The other one is having a beam's waist smaller than the aperture of the optical fibre. Those two conditions help in choosing the focal length of the collimation lens. Having a waist too big will result in a poor coupling efficiency (less than 50% for a single-mode fibre, less than 80% for a

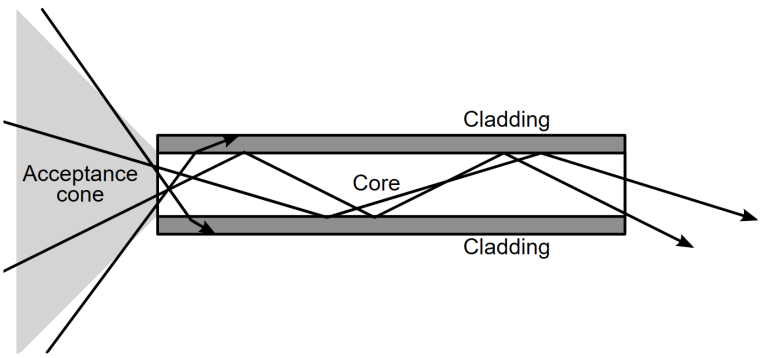

Figure 27: The acceptance cone is define by the critical angle depending on the refractive index of the core and cladding. This is one of the two coupling condition for an optical fibre.

multi-mode fibre). Having a part of the beam that is outside of the acceptance cone is the main other reason for such a loss.

D.2 Single versus multi-mode fibre

An optical fibre is imposing some boundary conditions on the transverse electro-magnetic field that is the coupled light. Those boundary conditions result in transverse mode conditions for the propagation called TEM_{pl} modes, p, l being respectively the angular and radial numbers of the Bessel function that is describing the beam in a cylindrical hypothesis. If the core diameter is less than ten times the light wavelength [37], the fibre is said to be single-mode. That is to say that the only propagative mode in this fibre is the TEM_{00} which is the well-known Gaussian mode. The coupling of such fibre is harder due to the diameter of the core and thus the difficulty one have to align properly the beam with the fibre.

D.3 Polarisation maintaining fibres

The polarisation maintaining optical fibre consists of a single-mode optical fibre that have built-in stress rod and a half-wave plate at its enter. Indeed, the optical fibre propagation mechanism is refractive index-dependent. Such an index is sensible to thermo-mechanical stress that can affect locally the fibre heterogeneously along its circumference. Thus, the different component of the light's polarisation can be transmitted at different velocity, rotating the beam's polarisation. Here, those rod creates a fast and slow axe of propagation. In those axis, the phase velocity of the light is very different from the one in the other axis making cross talking of the different modes impossible even under high stress. By aligning the light's polarisation to one of those two axis, the polarisation will be maintained at the exit of the optical fibre [38].